Numerical Heat Transfer, Part B, 39:617–635, 2001

1040-7790/01 $12.00 + .00

UNSTRUCTURED FINITE-VOLUME METHOD FOR RADIATIVE HEAT TRANSFER IN A COMPLEX TWO-DIMENSIONAL GEOMETRY WITH OBSTACLES

Man Young Kim, Seung Wook Baek, and Jae Hyun Park
Division of Aerospace Engineering, Department of Mechanical Engineering, Korea Advanced Institute of Science and Technology, Taejon, Korea

The radiative heat transfer in a complex two-dimensional enclosure with obstacles with participating medium is very important in practical engineering applications. In order to deal with this problem, in this study the finite-volume method (FVM) for radiation has been derived using the unstructured grid system. A general discretization equation was formulated by introducing the directional weight and the step scheme for spatial differencing. For its comparison and validation, two test cases, an equilateral triangular enclosure and a square enclosure with baffle, were chosen. Then, more complex and practical cases, such as a semicircular enclosure with cylinder hole, a square enclosure with finned internal cylinder, and a furnace with embedded cooling pipes, were investigated. All the results obtained by the unstructured FVM agreed very well with the exact solutions as well as the results obtained by the zone method. Furthermore, the wiggling behavior occurring in the blocked-off FVM was not produced by the unstructured FVM. Three types of manipulation of control angle overlap were also examined here. It was found that the solutions depended on the type of manipulation of control angle overlap, especially when the number of control angles was small. Usually, both the pixelation method and exact treatment introduced here yielded better solutions than the bold approximation.

INTRODUCTION

It is widely known that a prediction of radiative heat transfer in absorbing, emitting, and scattering media is one of prerequisite elements in analyzing and designing high-temperature equipment such as a boiler, furnace, pulverized coal combustor, or rocket propulsion system, for nowadays less pollutant emission as well as better efficiency is highly required in these systems to prevent environmental damage. Environmental regulations on pollutant species have become stricter due to concerns about acid rain and depletion of stratospheric ozone.

During the past decades, there has been much progress in various numerical techniques for solving the radiative transfer equation (RTE), which is integro-differential equation in nature. Among others, there are many recent works

Received 11 May 2000; accepted 22 November 2000.

Man Young Kim is currently at Diesel Engine Test Team 2, Namyang R&D Center, Hyundai Motor Company, Namyang-myun, Whasung-gun, Kyiunggi-Do 445-850, Korea.

Address correspondence to Prof. Seung Wook Baek, Division of Aerospace Engineering, Department of Aerospace Engineering, Korea Advanced Institute of Science and Technology, 373-1 Kusung-dong, Yusung-ku, Taejon 305-701, Korea. E-mail: swbaek@sorak.kaist.ac.kr

NOMENCLATURE

D_{ci}^{mn}	directional weights	σ_s	scattering coefficient
$\hat{e}_x, \hat{e}_y$	unit vector in x, y directions	Φ	scattering phase function
I	radiation intensity, $W/m^2\,sr$	ϕ	azimuthal angle
I_b	blackbody radiation intensity ($=\sigma T^4/\pi$), $W/m^2\,sr$	**Superscripts**	
$N_\theta(N_\phi)$	total number of polar (azimuthal) angles	$m(n)$	radiation direction of polar angle θ (azimuthal angle ϕ)
$\hat{n}_i$	unit normal vector at i surface	$m-, m+(n-, n+)$	starting and ending value of $m(n)$
q_w^R	wall radiative heat flux, W/m^2		
β_0	extinction coefficient ($=\kappa+\sigma_s$), m^{-1}		
$\Delta A_i, \Delta V$	surface area and volume of the control volume, respectively	**Subscripts**	
$\Delta\Omega^{mn}$	discrete control angle	i	incident quantity, face value
ε_w	wall emissivity	I	upwinding nodal point of P
θ	polar angle	P	nodal point in which intensities are located
κ	absorption coefficient, m^{-1}	w	wall
σ	Stefan-Boltzmann constant ($=5.67\times10^{-8}\,W/m^2\,K^4$)		

dealing with the radiation analysis in a complex geometry using the finite-volume method (FVM) or the discrete-ordinates method (DOM). Compared with the other methods such as Monte Carlo method, zone method, or P_N approximation, these two methods are known to be more compatible with the numerically discretized forms of momentum and energy equations in a nonorthogonal structured or unstructured grid system [1, 2].

The FVM for radiation, which is similar to the DOM, is a kind of flux method with flexible applicability to a complex geometry using an arbitrary control angle. In the FVM, the inflow and outflow of radiant energy across control-volume faces are balanced with attenuation and augmentation of radiant energy within a control volume and a control angle. Since its first introduction by Raithby and Chui [3], numerous applications have been found in two- and three-dimensional Cartesian and cylindrical coordinates [4].

In the past few years, an unstructured triangular mesh in two dimensions and a tetrahedral mesh in three dimensions have been widely accepted in computation, due to the ease of grid generation in complex and realistic geometries and the capability of grid adaptation [5]. Fiveland and Jesses [6] used the unstructured as well as the structured mesh to perform DOM as well as finite-element method (FEM) analysis of radiative heat transfer in a rectangular enclosure containing an absorbing/emitting medium. Recently, Mathur and Murthy [7] developed the unstructured FVM for radiation. They studied radiation-affected natural convection as well as the pure radiation problem using the unstructured grid system.

In rectangular geometry, the control angle is usually arranged by being laid tangent to a corresponding control-volume face. However, for the case of compu-

tation using an unstructured grid system, the control angle becomes overlapped, which is inevitable as in the nonorthogonal structured grid system. In the overlapped control angle, there exists a problem of overlapping of incoming and outgoing radiation so that careful attention must be exercised for accurate computation. In order to deal with this, Chai et al. [8] proposed a bold approximation, in which the whole control angle is assumed to be either incoming or outgoing, depending on the sign of its directional weight. Baek et al. [9] as well as Murthy and Mathur [7] suggested more accurate treatments. Whereas Baek et al. [9] divided the overlapped control angle into two parts by assigning incoming as well as outgoing intensity separately to satisfy the energy balance exactly, Murthy and Mathur [7] resolved the problem by pixelating the control angle.

In the present study, an extension of previous work by Baek et al. [9], the unstructured FVM for radiation is considered by adopting the triangular mesh. It is then validated by application to the analysis of radiative heat transfer in an irregular two-dimensional enclosure with obstacles such as baffles, pins, or pipes. To our best knowledge, the FVM for radiation has not yet been applied to a more realistic complex geometry as considered here. Furthermore, a more exact treatment of the control angle overlap is devised here for the application of the unstructured FVM. Its results are then compared with those obtained by the other two manipulations of control angle overlap, i.e., bold approximation and pixelation as mentioned above.

FORMULATIONS AND SOLUTION PROCEDURE

Radiative Transfer Equation (RTE)

The radiation intensity for a gray medium at any position $\mathbf{r}$ along a path $\hat{s}$ through an absorbing, emitting, and scattering medium is given by

$$\frac{1}{\beta_0}\frac{dI(\mathbf{r},\hat{s})}{ds} + I(\mathbf{r},\hat{s}) = (1-\omega_0)I_b(\mathbf{r}) + \frac{\omega_0}{4\pi}\int_{\Omega_i=4\pi} I(\mathbf{r},\hat{s}_i)\Phi(\hat{s},\hat{s}_i)\,d\Omega_i \tag{1}$$

where $\beta_0 = \kappa + \sigma_s$ is the extinction coefficient, $\omega_0 = \sigma_s/\beta$ is the scattering albedo, and $\Phi(\hat{s},\hat{s}_i)$ is the scattering phase function for radiation from incoming direction $\hat{s}_i$ to scattered direction $\hat{s}$. This equation, if the temperature field, $I_b(\mathbf{r})$, and boundary conditions for intensity are given, provides a distribution of the radiation intensity in the medium. The boundary condition for a diffusely emitting and reflecting wall can be denoted by

$$I(\mathbf{r}_w,\hat{s}) = \varepsilon_w I_b(\mathbf{r}_w) + \frac{1-\varepsilon_w}{\pi}\int_{\hat{s}_i\cdot\hat{n}_w<0} I(\mathbf{r}_w,\hat{s}_i)|\hat{s}_i\cdot\mathbf{n}_w|\,d\Omega_i \tag{2}$$

where ε_w is the wall emissivity and subscript w denotes the location of the wall, while $\hat{n}_w$ is the unit vector normal to it.

Unstructured Finite-Volume Method

To derive the discretized equation, Eq. (1) is integrated over a control volume (or cell), ΔV , and a control angle, $\Delta\Omega^{mn}$, as shown in Figure 1*a*. By assuming that

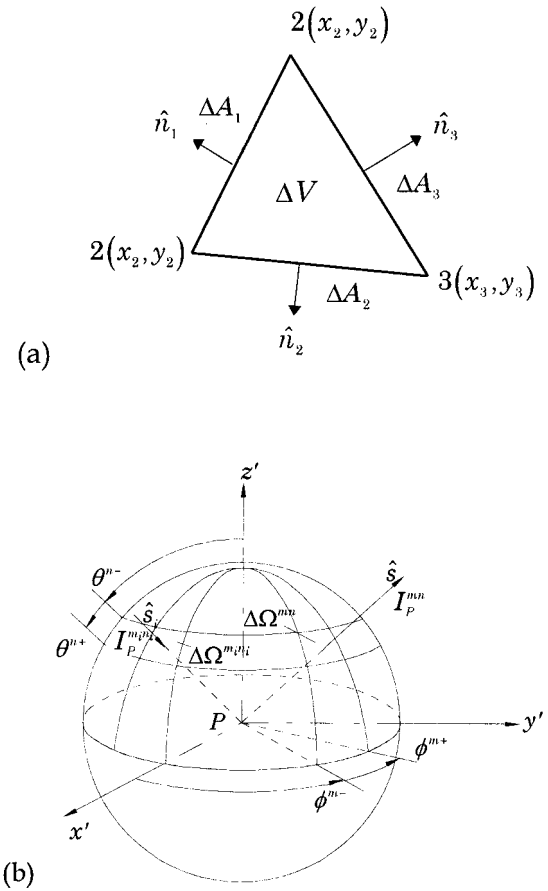

Figure 1. Schematics of control volume and control angle: (*a*) control volume; (*b*) control angle.

the magnitude of the intensity is constant but its direction varies within the control volume and control angle given, the following finite-volume formulation can be obtained:

$$\sum_{i=1,2,3} I_i^{mn}\,\Delta A_i\,D_{ci}^{mn} = \beta_0(-I^{mn} + S_R^{mn})_p\,\Delta V\,\Delta\Omega^m \tag{3}$$

where

$$D_{ci}^{mn} = \int_{\theta^{m-}}^{\theta^{m+}} \int_{\phi^{n-}}^{\phi^{n+}} (\hat{s}\cdot\hat{n}_i)\sin\theta\,d\theta\,d\phi \tag{4}$$

$$\hat{s} = \sin\theta\cos\phi\hat{e}_x + \sin\theta\sin\phi\hat{e}_y + \cos\theta\hat{e}_z \tag{5}$$

$$\hat{n}_i = n_{x,i}\hat{e}_x + n_{y,i}\hat{e}_y + n_{z,i}\hat{e}_z \tag{6}$$

$$S_R^{mn} = (1 - \omega_0)I_b + \frac{\omega_0}{4\pi}\int_{\Omega_i=4\pi} I^{m_i n_i}\Phi_{m_i n_i \to mn}\, d\Omega_i \tag{7}$$

$$\Delta\Omega^{mn} = \int_{\theta^{m-}}^{\theta^{m+}}\int_{\phi^{n-}}^{\phi^{n+}} \sin\theta\, d\theta\, d\phi \tag{8}$$

This equation indicates that a net outgoing radiant energy across the control-volume faces must be balanced by a net generation of radiant energy within the control volume and control angle.

The solid angle, 4π steradians, is discretized into $(N_\theta \times N_\phi)$ directions, where θ is a polar angle ranging from 0 to π and ϕ is an azimuthal angle ranging from 0 to 2π, as shown in Figure 1*b*. Although the control angle can be placed arbitrarily, usually it is equally divided such that $\Delta\theta^m = \theta^{m+} - \theta^{m-} = \pi/N_\theta$ and $\Delta\phi^n = \phi^{n+} - \phi^{n-} = 2\pi/N_\phi$. Once the angular limit for each control angle is fixed, the directional weight, which determines an inflow or outflow of radiant energy across the control-volume face depending on its sign, is evaluated as follows:

$$\begin{aligned} D_{ci}^{mn} = {} & [0.5\,\Delta\theta^m - 0.25(\sin 2\theta^{m+} - sin2\theta^{m-})] \\ & \times [n_{x,i}(\sin\phi^{n+} - \sin\phi^{n-}) + n_{y,i}(\cos\phi^{n+} - \cos\phi^{n-}) \\ & + 0.5n_{z,i}(\sin^2\theta^{m+} - sin^2\theta^{m-})\,\Delta\phi^n] \end{aligned} \tag{9}$$

Next, a scheme is required that relates a control-volume facial intensity to a nodal one. Among many others, here is adopted a step scheme in which a downstream facial intensity is set equal to the upstream nodal value. It not only ensures the positive intensity, but is also simple and convenient. For this scheme, a typical relation between facial and nodal intensities is as follows:

$$I_i^{mn} D_{ci}^{mn} = I_P^{mn} D_{ci,\,\mathrm{out}}^{mn} + I_I^{mn} D_{ci,\,\mathrm{in}}^{mn} \tag{10}$$

where $D_{ci,\,\mathrm{out}}^{mn}$ and $D_{ci,\mathrm{in}}^{mn}$ are varied depending on the manipulation of the control angle overlaps, which follows next. The overlaps can occur at interior as well as boundary face for the unstructured and nonorthogonal structured grid system [10].

Control Angle Overlaps

In order to understand the problem of control angle overlap, for which the incoming and outgoing intensities exist together for a given control angle, a simple example is considered. As shown in Figure 2*a*, control angles of $\Delta\Omega^2$ and $\Delta\Omega^6$ are overlapped so that the intensities in the range of (ϕ_A, ϕ^{2+}) and (ϕ^{6-}, ϕ_B) are incoming, while those in (ϕ^{2-}, ϕ_A) and (ϕ_B, ϕ^{6+}) are outgoing. In order to manage this overlapped angle, three types of manipulation are considered here, as depicted in Figures 2*b*, 2*c*, and 2*d*. While the first and second ones are named as the bold approximation [8] and the pixelation method [7] respectively, the third one that is newly proposed here is termed the exact treatment [9].

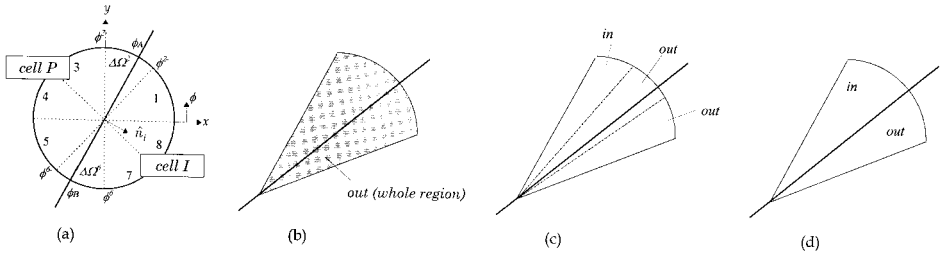

Figure 2. Manipulations of control angle overlaps: (*a*) top view of overlapped control angle; (*b*) bold approximation; (*c*) pixelation method ($N_p = 3$); (d) exact treatment.

Bold Approximation

Chai et al. [8] performed a bold approximation, in which a solid angle is assumed wholly either outgoing or incoming depending on the sign of its directional weight. The schematic of this simple method is presented in Figure 2*b*. The facial value is, then, determined as follows:

$$I_i^{mn} D_{ci}^{mn} = I_P^{mn} \max(D_{ci}^{mn}, 0) - I_I^{mn} \max(-D_{ci}^{mn}, 0) \tag{11}$$

or

$$I_i^{mn} D_{ci}^{mn} = I_P^{mn} D_{ci,\text{out}}^{mn} + I_I^{mn} D_{ci,\text{in}}^{mn} \tag{12}$$

where

$$D_{ci,\text{out}}^{mn} = \max(D_{ci}^{mn}, 0) \qquad D_{ci,\text{in}}^{mn} = -\max(-D_{ci}^{mn}, 0) \tag{13}$$

Pixelation Method

In the pixelation method, only the overlapped control angle is pixelated, while the other angles still adopt the bold approximation. Within the overlapped angle, the bold approximation is applied to each pixelated angle. Figure 2*c* shows a schematic of this method with three pixelations of the control angle given. Since the two-dimensional problem is considered in the present study, the pixelation process is introduced to the azimuthal angle only. If the number of pixelation is N_p, then the total number of control angle becomes $N_p = 1$. When $N_p = 1$, this becomes $N_\theta X N_p$ that is the bold approximation. This pixelation process is very similar to the grid adaptation used in computational fluid dynamics (CFD).

Exact Treatment

The common shortcoming for the above two methods is not to keep the energy balance conserved between energy inflow and outflow for the overlapped angle. The pixelation method satisfies the energy balance only when the number of pixelation is very large such that $N_p \gg 1$.

Recently, Baek et al. [9] overcame such a shortcoming by dividing the overlapped angle into two parts and assigned an incoming or outgoing intensity to each as shown in Figure 2*d*. Then, the facial intensity becomes:

$$I_i^{mn} D_{ci}^{mn} = I_p^{mn} D_{ci,\text{out}}^{mn} + I_I^{mn} D_{ci,\text{in}}^{mn} \tag{14}$$

where

$$D_{ci,\text{out}}^{mn} = \int_{\Delta\Omega^{mn}} (\hat{\zeta} \cdot \hat{n}_i)\, d\Omega \quad \hat{s} \cdot \hat{n}_i > 0 \tag{15}$$

$$D_{ci,\text{in}}^{mn} = \int_{\Delta\Omega^{mn}} (\hat{\zeta} \cdot \hat{n}_i)\, d\Omega \quad \hat{s} \cdot \hat{n}_i < 0 \tag{16}$$

In this exact method, the total number of control angles becomes $N_\theta(2 + N_\phi)$.

Linear Solver

Considering all the supplementary equations above, Eq. (3) can be recast into the following linear equation:

$$a_p^{mn} I_p^{mn} = \sum_{I=1,2,3} a_I^{mn} I_I^{mn} + b_p^{mn} \tag{17}$$

where

$$a_I^{mn} = -\Delta A_i D_{ci,\text{in}}^{mn} \tag{18}$$

$$a_P^{mn} = \sum_{i=1,2,3} \Delta A_i D_{ci,\text{out}}^{mn} + \beta_{0,P}\, \Delta V\, \Delta\Omega^{mn} \tag{19}$$

$$b_P^{mn} = (\beta_0 S_R^{mn})_P\, \Delta V\, \Delta\Omega^{mn} \tag{20}$$

The boundary condition in Eq. (2) for a diffusely emitting and reflecting wall can be discretized by

$$I_w^{mn} = \varepsilon_w I_{bw} + \frac{1 - \varepsilon_w}{\pi} \sum_{\hat{s}_i \cdot \hat{n}_w < 0} I_w^{m_i n_i} |D_{cw,\text{in}}^{m_i n_i}| \qquad \hat{s}_i \cdot \hat{n}_w > 0 \tag{21}$$

where

$$D_{cw,\text{in}}^{mn} = \int_{\Delta\Omega^{mn}} (\hat{s} \cdot \hat{n}_w)\, d\Omega \qquad \hat{s} \cdot \hat{n}_w < 0 \tag{22}$$

is the directional weight at the bounding wall.

The iterative procedure using Eq. (17) is terminated when the following convergence is attained:

$$\max(|I_P^{mn} - I_P^{mn,\text{old}}|/I_P^{mn}) \le 10^{-6} \tag{23}$$

where $I_P^{mn,\text{old}}$ is the previous iteration value of I_P^{mn}. Once the intensity field is

obtained, the wall radiative heat flux can be estimated as follows:

$$q_w^R = \int_{\Omega=4\pi} I(\hat{r}_w, \hat{s})(\hat{s} \cdot \hat{n}_w)\, d\Omega = \sum_{n=1}^{N_\phi} \sum_{m=1}^{N_\theta} I_w^{mn}(D_{cw,\text{in}}^{mn} + D_{cw,\text{out}}^{mn}) \tag{24}$$

which is the positive when net heat is transferred from the wall to medium.

Geometric Relations

In order to close the general discretization equation (17), the volume of the control volume (or cell), ΔV, surface area, ΔA_i, and outward unit normal vector, $\hat{n}_i$, have to be provided. According to notations in Figure 1*a*, the product of the unit normal vector and surface area can be represented by

$$\begin{pmatrix} \Delta A_1 \hat{n}_1 \\ \Delta A_2 \hat{n}_2 \\ \Delta A_3 \hat{n}_3 \end{pmatrix} = \begin{pmatrix} y_2 - y_1 \\ y_3 - y_2 \\ y_1 - y_3 \end{pmatrix} \hat{e}_x - \begin{pmatrix} x_2 - x_1 \\ x_3 - x_2 \\ x_1 - x_3 \end{pmatrix} \hat{e}_y \tag{25}$$

and the volume of the triangular cell can be given by

$$\Delta V = \sqrt{s(s - \Delta A_1)(s - \Delta A_2)(s - \Delta A_3)} \tag{26}$$

where

$$s = \frac{1}{2} \sum_{i=1}^{3} \Delta A_i \tag{27}$$

RESULTS AND DISCUSSIONS

In the present study, five test cases are considered. The results obtained are presented and discussed in separate sections.

An Equilateral Triangular Enclosure

First, the unstructured FVM is applied to an equilateral triangular enclosure with an absorbing and emitting, but nonscattering, medium maintained at constant temperature of $T_g = 1,000\,\text{K}$ as shown in Figure 3*a*. The length of each side is 1 m and the walls are held cold ($T_w = 0\,\text{K}$) and black ($\varepsilon_w = 1.0$). In this case, the intensity, which is exact at any location within the enclosure, may be obtained by summing all the intensities from the enclosure wall as well as local emission by the medium such that

$$I(s) = I_{bw} e^{-\kappa s} + I_b(1 - e^{-\kappa s}) \tag{28}$$

where I_b is the local blackbody intensity of the medium and s is the path length. Then, the exact wall heat flux can be obtained by numerically integrating $I(s)(\hat{s} \cdot \hat{n}_w)$ over all incident solid angles via Gaussian quadrature numerical integration [9]. The relative average error of radiant heat fluxes on a wall is calculated for comparison as

$$\text{Error} = \sum_{\text{nods}} \frac{|q_{\text{cal}} - q_{\text{exact}}|/q_{\text{exact}}}{\text{number of wall nodes}}$$

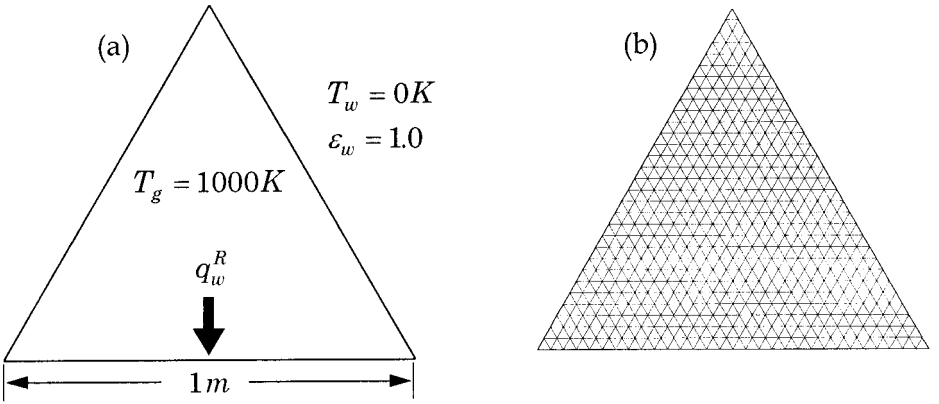

Figure 3. An equilateral triangular enclosure: (*a*) schematic; (*b*) spatial grid system with 900 cells and 496 nodes.

where q_{cal} is the calculated value and q_{exact} is the exact value.

Figure 3*b* shows the spatial grid system consisting of 900 cells and 496 nodes. The dimensionless incident radiative heat flux onto the bottom wall is presented in Figure 4 with the absorption coefficient of $1\,\text{m}^{-1}$. Two kinds of angular discretization, $(N_\theta \times N_\phi) = (4 \times 8)$ and (4×16), and three types of manipulation of control angle overlap are examined here. The number of pixelations is chosen to be 2 when the control angle is pixelated. When the angular discretization is $(N_\theta \times N_\phi) = (4 \times 16)$, the results well match the exact solution regardless of how we deal with the problem of control angle overlap. However, for the case of $(N_\theta \times N_\phi) = (4 \times 8)$, the exact treatment and the pixelation method produce better results than the bold approximation. The relative average errors and corresponding computing times for three types of angular manipulations are compared in Table 1. The values in parentheses represent a computational time required for each type calculation, for which the unit is not important since it is machine-dependent. For the case of $(N_\theta \times N_\phi) = (4 \times 8)$, the pixelation method as well as the exact treatment yields 2% increase in accuracy with 22% increase in computational time over the bold approximation. When the angular discretization is $(N_\theta \times N_\phi) = (4 \times 16)$, it results in 41% increase in accuracy with 100% increase in computational time for the bold approximation, and 41% increase in accuracy with 140% increase in computational time for the pixelation method and the exact treatment.

A Square Enclosure with Baffle

The next topic to consider here is related to a square enclosure with baffle as shown in Figure 5*a*, which has been studied previously by Coelho et al. [11] using the structured DOM and the discrete transfer method (DTM). The baffle, suspended on the top wall, is 0.01 m wide and 0.4 m long. All the surrounding walls as well as a baffle exert unit emissive power and are assumed to be blackbodies. The nonscattering gray medium has an absorption coefficient of $\kappa = 1\,\text{m}^{-1}$ and an

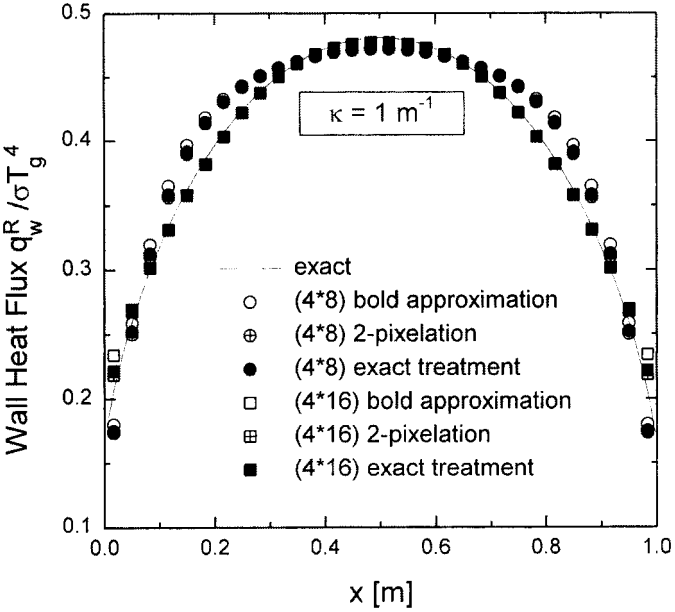

Figure 4. Comparison of radiative heat flux q_w^R onto the bottom wall of an equilateral triangular enclosure.

Table 1. Comparison of relative error and computing time for the equilateral triangular enclosure with $\kappa = 1.0\,\mathrm{m}^{-1}$

	$(N_\phi \times N_\theta)$	
	(4×8)	(4×16)
Bold approximation	0.04819 (22)	0.02844 (44)
Pixelation method ($N_{\mathrm{pix}} = 2$)	0.04709 (27)	0.02838 (66)
Exact treatment	0.04719 (28)	0.02825 (65)

Arbitrary time unit depending on machine.

emissive power of $E_{bg} = 10\,\mathrm{W/m^2}$. The spatial grid system depicted in Figure 5*b* consists of 2,208 cells and 1,196 nodes with an angular grid system of $(N_\theta \times N_\phi) = (4 \times 32)$. The incident heat flux is calculated along the enclosure in the direction s using the unstructured FVM with three types of manipulations of control angle overlap. It is plotted in Figure 6 and compared with the others obtained by using the zone method and the FVM [12] and DOM [11] which adopted a structured blocked-off grid system. Hereafter, "unstructured grid" is abbreviated as "UNS" in the figures for brevity. Compared with the results obtained by the zone method, the unstructured mesh produces good agreement. As in the previous

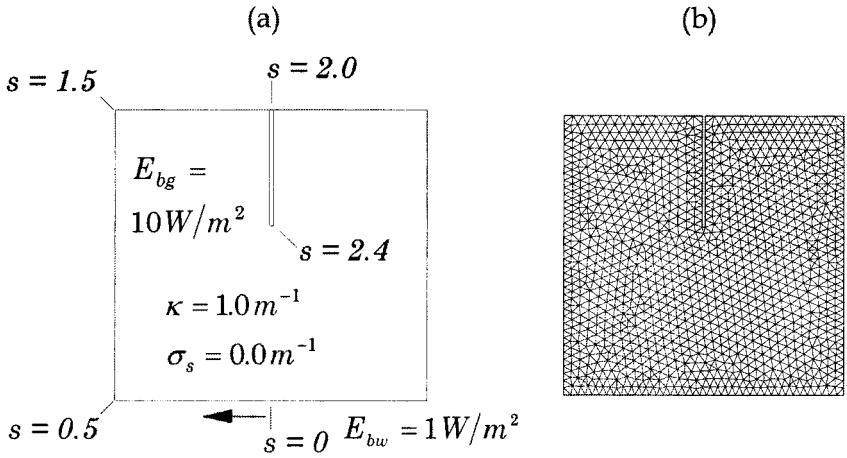

Figure 5. A square rectangular enclosure with baffle: (*a*) schematic; (*b*) spatial grid system with 2,208 cells and 1,196 nodes.

equilateral triangle case, different manipulation of the control angle overlap is seen not to make any difference in the results, since the angular discretization used here is sufficiently fine. Compared with the case without a baffle, the baffle reduces the net heat flux, for the presence of the baffle hinders the radiant energy transfer from the hot medium to the wall boundary.

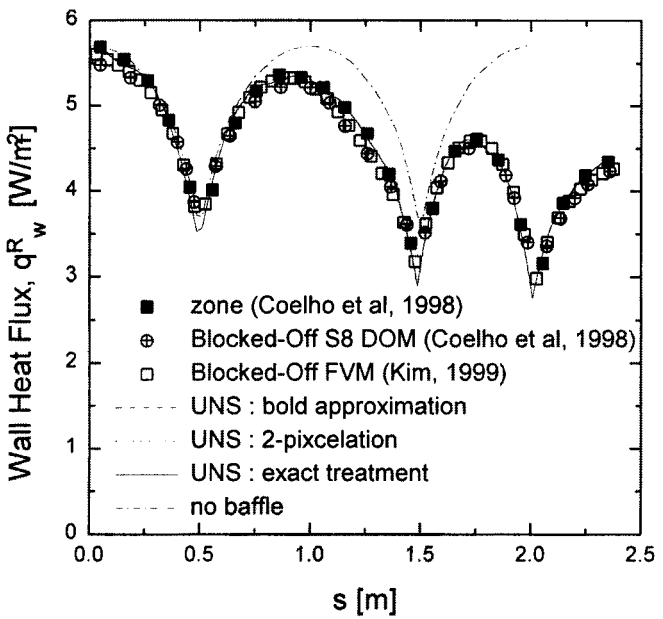

Figure 6. Comparison of radiative heat flux q_w^R along the boundary of a square enclosure with baffle.

A Semicircle Enclosure with Circular Hole

Based on the validation of the present unstructured FVM solver as above, a semicircle enclosure with one circular hole as an example of a more complex configuration, which has not been considered before, is now examined. As presented in Figure 7, a circular hole 0.2 m in radius is located at $y = 0.4$ m inside a semicircle enclosure with $R_0 = 1$ m. The medium enclosed is absorbing as well as emitting with a uniform temperature of $T_g = 1{,}000$ K, while all other boundaries are cold and blackbody. The spatial grid system used consists of 1,346 cells and 733 nodes with $(N_\theta \times N_\phi) = (4 \times 16)$.

Figure 8 depicts the incident radiative heat flux distribution along the bottom wall for various absorption coefficients. For $\kappa = 10\,\mathrm{m}^{-1}$, the dimensionless radiative

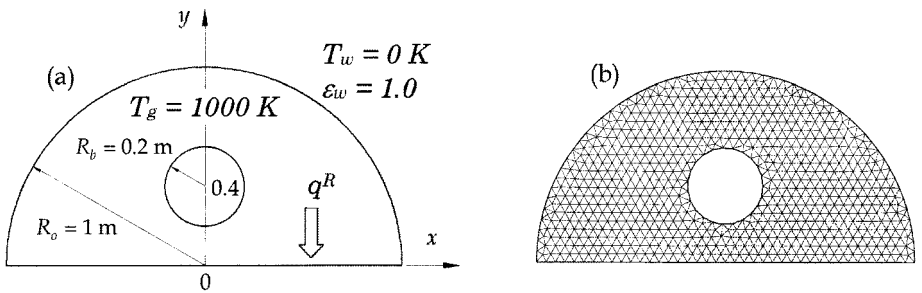

Figure 7. A hemispherical enclosure with circular hole: (*a*) schematic; (*b*) spatial grid system with 1,346 cells and 733 nodes.

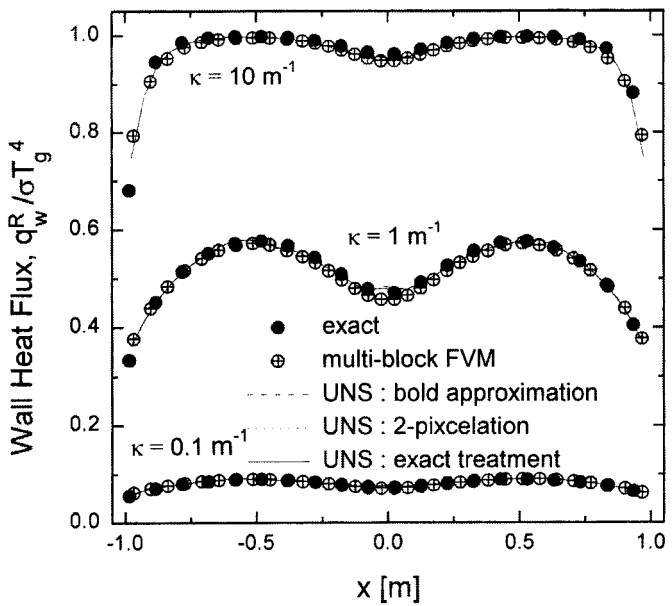

Figure 8. Comparison of radiative heat flux q_w^R onto the bottom wall of a hemispherical enclosure with a circular hole.

heat flux along the bottom wall is near unity except at the center and the side corner, because the incident radiation on the wall derives mainly from the neighboring hot medium rather than from the inner medium, away from the wall. Therefore, the medium temperature near the wall is lower, while the inner medium temperature is higher. Near the side corner, however, the radiative heat flux decreases rapidly, since that is the place where the cold walls meet each other. As the absorption coefficient decreases, the radiative heat flux at the bottom wall is significantly reduced. This is because the emissive power of the medium is reduced since the absorption coefficient is smaller. For this smaller absorption coefficient, the temperature is more uniformly distributed from the near wall to the inner medium. Results obtained by the unstructured FVM as well as the structured multiblock method are in good agreement with the exact solution.

A Square Enclosure with Finned Internal Cylinder

As a further application of the present unstructured FVM code to a new geometry, a square enclosure with a finned cylinder is now examined. Only a quarter section of its schematic is shown in Figure 9, where $L_x = L_y = 1\,\text{m}$, $H = 0.25\,\text{m}$, $W = 0.1\,\text{m}$, and $R = 0.5\,\text{m}$. The enclosed medium is in radiative equilibrium with either $\beta_0 = 0.1\,\text{m}^{-1}$, $\omega_0 = 0.7$, or $\beta_0 = 5.0\,\text{m}^{-1}$, $\omega_0 = 0.7$. While the temperature of the outer square is held at 300 K, the inner finned cylinder temperature is 1,000 K. All the walls including fins are assumed to be blackbody. The spatial grid system adopted in this calculation is composed of 2,238 equal-sized triangular cells and 1,206 nodal points. The entire angular domain is discretized into $(N_\theta \times N_\phi) = 4 \times 12$ control angles with equal $\Delta\theta$ and $\Delta\phi$.

The results obtained by the bold approximation and exact UNS are compared with those by the blocked-off finite-volume method (FVM), which is another

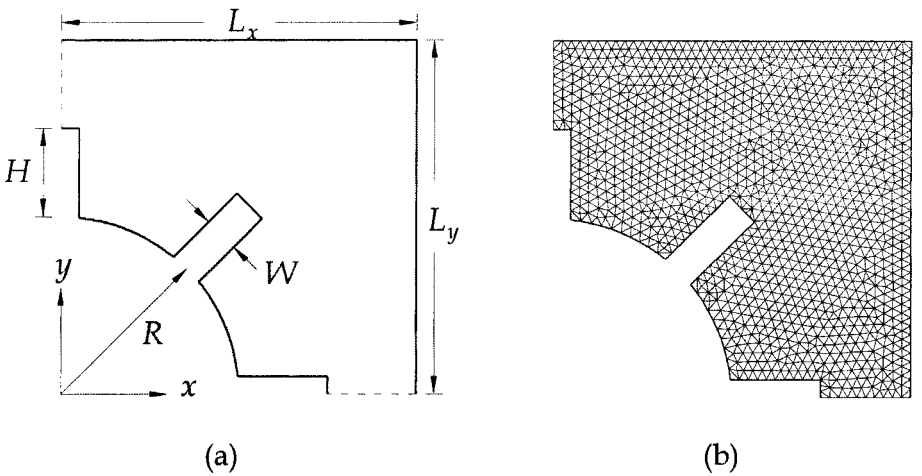

Figure 9. A square enclosure with finned internal cylinder: (*a*) schematic; (*b*) spatial grid system with 2,238 cells and 1,206 nodes.

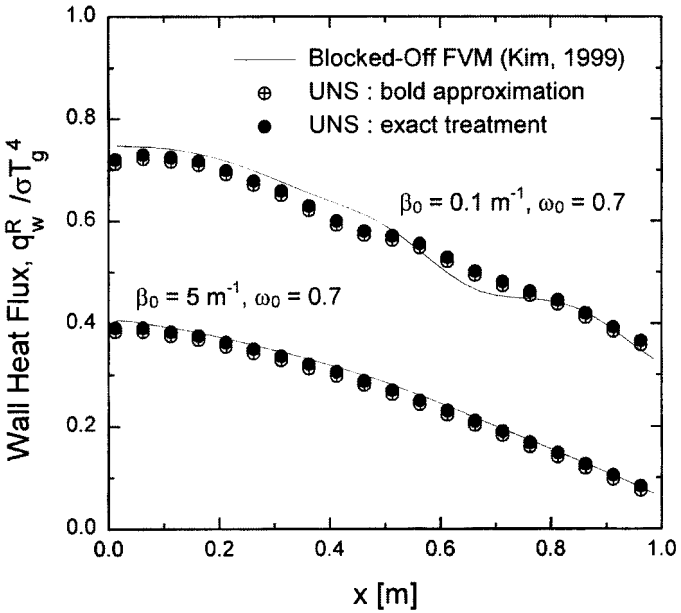

Figure 10. Comparison of radiative heat flux q_w^R onto the top wall of a square enclosure with a finned internal cylinder.

numerical tool for a complex geometry [12]. As depicted in Figure 10, the radiative heat flux onto the top wall decreases with increasing extinction coefficient, due to the radiative heat blockage effect of the medium. For the case of $\beta_0 = 0.1\,m^{-1}$, the effect of the finned cylinder is apparent in that there is a minor dent in the radiative heat flux variation obtained by UNS. The solution obtained by the blocked-off FVM is seen to be a little poorer than that by UNS. This can be elucidated in Figure 11, which illustrates isothermal contours for the conditions given above. The isothermal line near the cylinder produced by the blocked-off FVM is shown to be wiggled. However, for the case of $\beta_0 = 5\,m^{-1}$, the effect of the finned cylinder is not clear, since the incident heat flux is influenced mainly by the radiation field in the vicinity of the square wall for higher absorption coefficient. In Figure 11 the temperature difference between the adjacent isothermal lines is 100 K. Therefore, for the case of $\beta_0 = 0.1\,m^{-1}$ the temperature gradient is seen to be steep in the vicinity of the square wall. It is also noted that the wiggling behavior does not occur in the solutions obtained by the UNS.

A Furnace with Embedded Cooling Pipes

Finally, a geometric model of a furnace is considered, which is similar to the three-dimensional one of Adams and Smith [13], who analyzed the radiative heat transfer using the discrete-ordinates method. In the present example, however, the furnace is simplified as a two-dimensional enclosure 2.0 m in width and 6.29 m

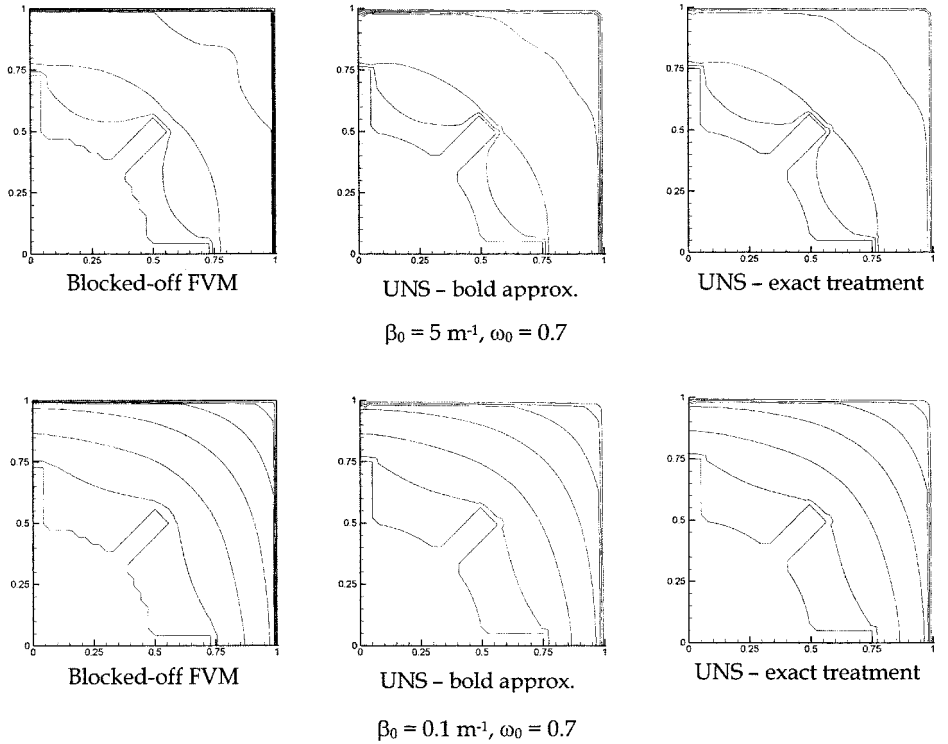

Figure 11. Isothermal lines.

in length, as presented in Figure 12. There exist 22 cooling pipes along the top wall between 2.22 and 6.29 m. The pipe, 0.03 m in diameter, is 0.025 m away from the top wall. The furnace wall and pipe emissivities are 0.5 and 0.8, respectively. The furnace wall and gas medium temperatures are obtained from the work by Michelfelder and Lowes [14], while the cooling pipe temperature is assumed to be 300 K. It is depicted in Figure 13. At the point where a measured value does not exist, the temperature is calculated by interpolating the neighboring data. Gas absorption coefficient is set to be $0.2\,m^{-1}$. The spatial grid system used has 26,718 cells and 9,207 nodes, while $N_\theta = 2$ in polar and $N_\phi = 8$ in azimuthal angle direction for the total 4π steradian solid angle.

Figure 14 shows the incident radiative heat flux distribution along the top wall. It is shown to be dramatically fluctuating where the cooling pipes exist, since they intercept incident radiation coming from the hot medium toward the wall. The heat flux along the top wall in the region of $4\,m < x < 5\,m$ is enlarged for comparison of various methods and is drawn in Figure 15. The blocked-off FVM is seen to be as good as the unstructured FVM. Different types of control angle overlap manipulation make only a minor difference. This is because the number of control angles is sufficient. As the number of control angles decreases, the effects of different control angle overlap manipulations would not be negligible.

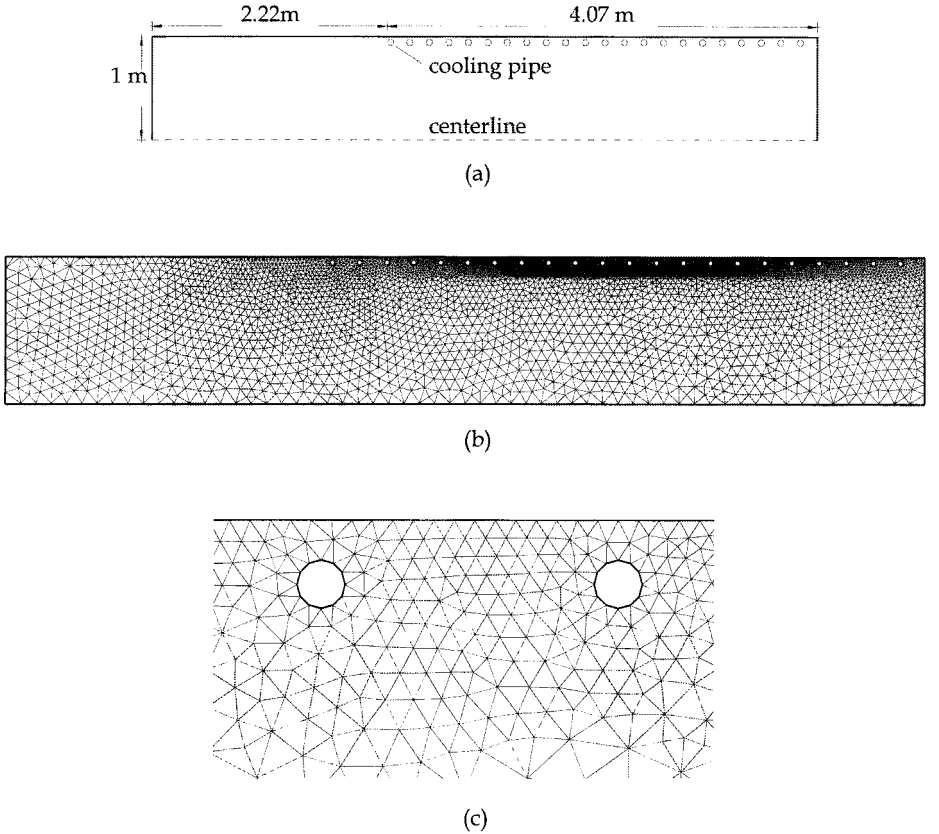

Figure 12. A furnace with embedded cooling pipes: (*a*) schematic; (*b*) spatial grid system with 26,718 cells and 9,207 nodes; (*c*) enlarged view of grid system near the cooling pipes.

CONCLUSIONS

In this study the unstructured finite-volume method has been developed for more realistic application to analyzing the radiative heat transfer in a more complex enclosure with obstacles. The final form of the general discretization equation was derived here using the directional weight and the step scheme. Simultaneously, in order to deal with the problem of control angle overlap, three types of manipulation, the bold approximation, the pixelation method, and the exact treatment, were considered. Since the main objective of this work was to seek the compatibility of the unstructured FVM for radiation with the other discretized governing equations such as momentum and energy equations, the nodal points and cells used therein were chosen. Then, this method was applied to such diverse examples as an equilateral triangular enclosure, a square enclosure with a baffle, a semicircular enclosure with a cylindrical hole, a square enclosure with a finned internal cylinder, and a furnace with embedded cooling pipes. For the concrete validation for the former two cases, the current results were compared with exact solutions or those

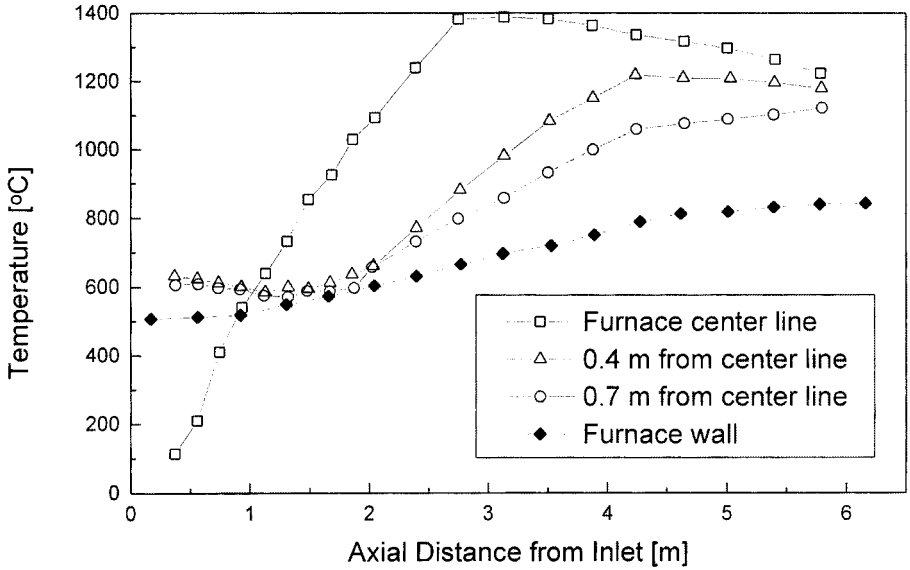

Figure 13. Temperature distribution of furnace.

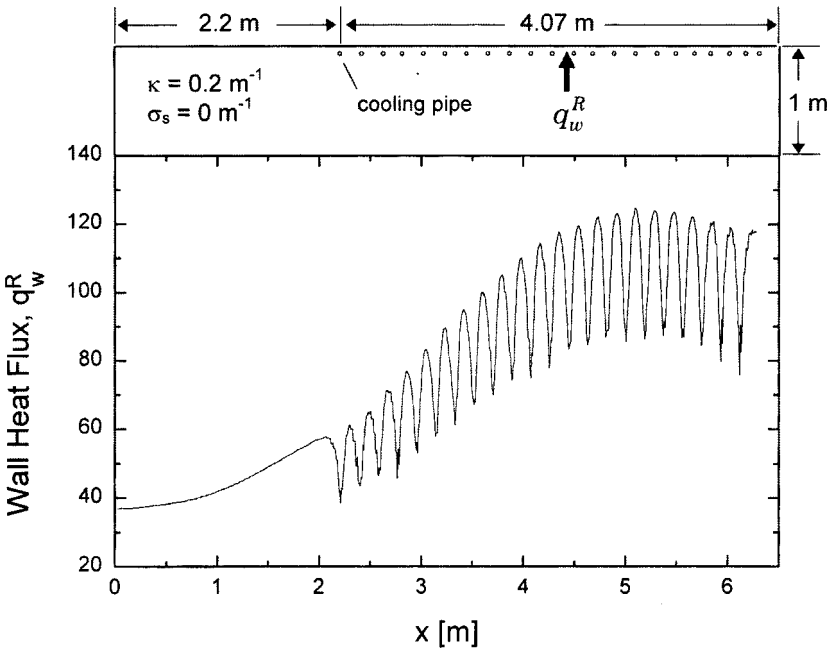

Figure 14. Distribution of the radiative heat flux q_w^R along the top wall of a furnace with embedded cooling pipes.

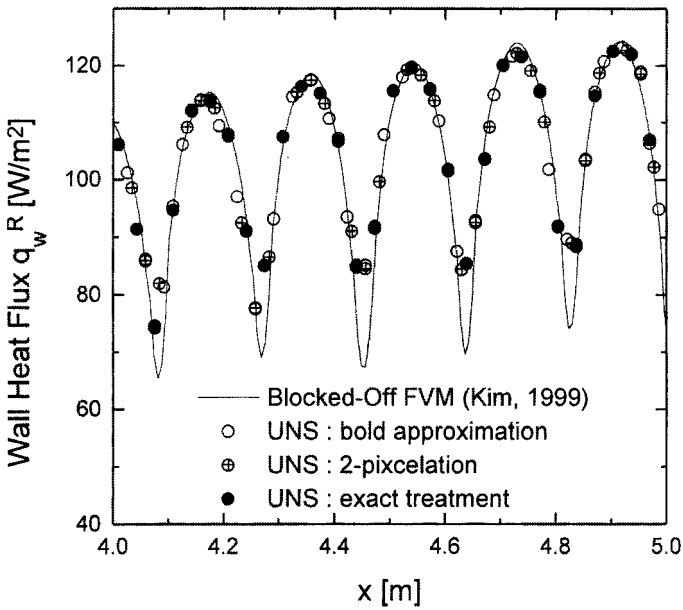

Figure 15. Comparison of radiative heat flux q_w^R onto the top wall of a furnace with embedded cooling pipes for 4.0 m $< x <$ 5.0 m.

obtained by other numerical techniques such as the zone method and the multiblock or blocked-off FVM with structured mesh. Then, more complex configurations for the latter three were examined. The unstructured FVM derived here was found not to show wiggling behavior in the computed results, which occurred in the blocked-off structured grid system. It was also found that the solutions depended on the type of manipulation of control angle overlap, especially when the number of control angles was small. Usually, both the pixelation method and exact treatment yielded better solutions than the bold approximation.

REFERENCES

1. E. H. Chui and G. D. Raithby, Computation of Radiant Heat Transfer on a Nonorthogonal Mesh Using the Finite Volume Method, *Numer. Heat Transfer B*, vol. 23, pp. 269–288, 1993.
2. G. D. Raithby, Discussion of the Finite Volume Method for Radiation and Its Application Using 3D Unstructured Meshes, *Numer. Heat Transfer B*, vol. 35, pp. 389–405, 1999.
3. G. D. Raithby and E. H. Chui, A Finite-Volume Method for Predicting a Radiative Heat Transfer in Enclosures with Participating Media, *ASME J. Heat Transfer*, vol. 112, pp. 415–423, 1990.
4. E. H. Chui, G. D. Raithby, and P. M. J. Hughes, Prediction of Radiative Transfer in Cylinderical Enclosures with the Finite Volume Method, *AIAA J. Thermophys. Heat Transfer*, vol. 6, pp. 605–611, 1992.
5. O. J. Kwon, Three-Dimensional Unstructured Grid Eular Method Applied to Turbine Blades, *Comput. Fluid Dynam. J.*, vol. 14, pp. 165–176, 1995.

6. W. A. Fiveland and J. P. Jessee, Finite Element Formulation of the Discrete-Ordinates Method for Multidimensional Geometries, *AIAA J. Thermophys. Heat Transfer*, vol. 8, pp. 426–433, 1994.
7. J. Y. Murthy and S. R. Mathur, Finite Volume Method for Radiative Heat Transfer Using Unstructured Meshes, *AIAA J. Thermophys. Heat Transfer*, vol. 12, pp. 313–321, 1998.
8. J. C. Chai, H. S. Lee, and S. V. Patankar, Finite Volume Method for Radiation Heat Transfer, *AIAA J. Thermophys. Heat Transfer*, vol. 8, pp. 419–425, 1994.
9. S. W. Baek, M. Y. Kim, and J. S. Kim, Nonorthogonal Finite-Volume Solutions of Radiative Heat Transfer in a Three-Dimensional Enclosure, *Numer. Heat Transfer B,* vol. 34, pp. 419–437, 1998.
10. S. R. Mathur and J. Y. Murthy, Radiative Heat Transfer in Periodic Geometries Using a Finite Volume Scheme, *ASME J. Heat Transfer*, vol. 121, pp. 357–364, 1999.
11. P. J. Coelho, J. M. Goncalves, and M. G. Carvalho, Modeling of Radiative Heat Transfer in Enclosures with Obstacles, *Inter. J. Heat Mass Transfer*, vol. 41, pp. 745–756, 1998.
12. M. Y. Kim, Combustion Characteristics in a Three-Dimensional Gas-Fired Combustion Chamber with Radiation Effect, Ph.D. thesis, Department of Aerospace Engineering, KAIST, Taejon, Korea, 1999.
13. B. R. Adams and P. J. Smith, Three-Dimensional Discrete-Ordinates Modeling of Radiative Transfer in a Geometrically Complex Furnace, *Combustion Sci. Technol.*, vol. 88, pp. 293–308, 1993.
14. S. Michelfelder and T. M. Lowes, Report on the M-2 Trials, IFRF Doc. No. F36/a/4, Ijmuiden, The Netherlands, 1988.